FLOW INSTABILITY AROUND A 2D AIRFOIL INDUCED BY ACOUSTIC DISTURBANCES AT LOW REYNOLDS NUMBERS

Takashi Atobe, Tomoaki Ikeda
Japan Aerospace Exploration Agency

Keywords: *Computational Fluid Dynamics, Flow Stability, Aeroacoustics*

Abstract

In this paper, a numerical study is presented to investigate a boundary-layer instability on the suction side of a NACA0006 airfoil, induced by aerodynamic sound scattered from a trailing-edge. By incorporating a linear stability analysis into the direct simulations with a compressible Navier-Stokes code using high-order accurate schemes, the unsteady characteristics are estimated upon resolving the acoustic effects of trailing-edge noise generation. The onset condition of an acoustic feedback loop is explored by altering the Mach number, compared with the frequency characteristics of the boundary-layer instability. While increasing the Mach number prompts the excitation of the feedback loop via the amplification of acoustic disturbances, the instability of the boundary layer seems to be suppressed at a higher Mach number; therefore, the onset condition should be determined between these two contradictory features, at a given Mach number. Also the phase requirement between acoustic and hydrodynamic waves is closely examined to attain a feedback loop. It is strongly suggested that this phasing consistency should explain the presence of discrete resonance modes. In the present result, however, the mechanism to determine the discrete frequencies is still an open question for future research.

1   Introduction

Trailing-edge (TE) noise is one of major tonal noises emitted from an airplane. Noise-source eddies develop near the trailing edge of an airfoil with time-periodic structures to achieve narrowband spectra. Then a tonal sound is scattered therefrom, much more efficiently than a direct radiation from the noise source itself. Up to now, this phenomenon has been studied on many aspects. In a moderate range of Reynolds (Re) numbers, of the order of 10^5 to 10^6, it is postulated that the noise generation process is deeply related with a self-induced feedback mechanism: Tollmien-Schlichting (T-S) unstable waves, originally induced by acoustic disturbances scattered from TE, develop into an organized vortical motion in the region near TE on the pressure side of the airfoil, where a separation bubble should be formed. Then, a tonal noise is generated as the vortices are shed from TE, which would again induce T-S waves, and eventually form a closed loop. This postulation, originally proposed by [12], has been verified via several experimental studies [7, 8]. Then, it is naturally assumed that the establishment of the acoustic feedback loop should require the phase consistency between sound waves traveling upstream from TE, and hydrodynamic T-S waves that propagate downstream at a phase velocity U_c, which is the order of base-flow velocity, U. This phase conformation requirement is also utilized to explain the "ladder-like" discrete frequency variation, which has the dependence of the noise frequency $f \propto U^{0.8}$, observed by [9].

On the other hand, it is also pointed out by the experimental observations referenced above, that presumably f follows the scaling of $U^{3/2}$ in average, in the discontinuous shift between

the ladder-like modes. This scaling law is derived from a dimensional analysis of wake configurations with velocity deficits behind an airfoil [10]. In the original derivation, self-excited vortex shedding is studied for bluff bodies, by proposing the universal Strouhal number defined from proper physical scales in wake profiles. If we assume that self-induced unsteadiness is prompted by such wake characteristics, the primary frequency should be determined mathematically as a singular solution of the stability theory [1, 6]. However, it is not very clear how these two different instability mechanisms, the T-S wave amplification in the boundary layer, and the wake-flow instability with mathematical singularity, affect each other in a closed feedback loop to reach discrete tones.

There are also many numerical studies available on TE noise generation. Among them, Desquesnes et al. [2] investigated the discrete noise generation process of the NACA0012 airfoil at $Re = 2 \times 10^5$ on a two-dimensional grid configuration. They claimed that the discrete tones are produced via the interaction of vortices shed from both sides of the airfoil, while the main feedback loop occurs on the pressure side at the Reynolds number. The DNS study by Sandberg et al. [11] also conducted two-dimensional calculations of NACA symmetric airfoils at $Re = 5 \times 10^4$. Their intention was to examine the acoustic field by artificially imposing T-S waves. The present authors also conducted two-dimensional DNS of a NACA0006 airfoil at $Re = 2 \times 10^4$. In our study, it was shown that an acoustic feedback loop may arise by increasing an inflow Mach number, which results in amplifying imposed acoustic disturbances [3]. Although the wake instability is presumably dominant at a low Reynolds number, the onset of an acoustic feedback loop induces a noticeable vortical fluctuation in the suction-side boundary layer, and eventually alters the vortex shedding pattern.

In this paper, our aim is first to investigate the TE noise generation driven with the acoustic feedback loop at a low Reynolds number. Acoustic fields are reproduced simultaneously on hydrodynamic flow motions by using compressible
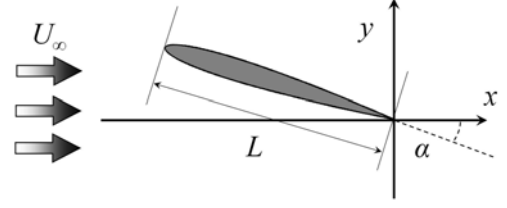

Fig. 1 Flow configuration for NACA0006 airfoil.

direct simulation techniques. The onset condition of a feedback loop is examined from the view point of boundary-layer stability. Particularly, the flow Mach number has an effect on both the acoustic wave scattered from TE, and the base flow compressibility. By increasing M, acoustic disturbances are amplified to stimulate the boundary-layer instability mechanism, while the shear flow is usually stabilized at higher Mach numbers. It is of interest to clarify the Mach number effect on the TE noise generation, also by the use of a linear stability analysis. The boundary-layer instability is quantitatively evaluated on tonal frequencies obtained in the flow solver. Secondly, the mechanism of discrete-tone generation is examined in conjunction with an acoustic feedback loop. To form a feedback loop via acoustic disturbances, the phase arrangement must be determined properly to attain a resonance between sound waves and hydrodynamic waves in the boundary layer. This requirement is supposed to introduce discrete modes in TE noise generation. It is also reported that multiple discrete tones coexist at a moderate Reynolds number, of the order of 10^5 as in [2], which would explain the ladder-like structure on frequency determination. Here we would also clarify the development of discrete modes in the two-dimensional airfoil flow at a low Reynolds number.

2 Numerical Method and Conditions

We solve the set of two-dimensional compressible Navier-Stokes (N-S) equations. Fluid property is assumed to be of air; its specific-heat ratio is treated to be constant, 1.4. A symmetric NACA four-digit airfoil, 0006 is employed for unsteady

simulations in our study. The geometric configuration is shown in Fig. 1. The chord length L is used as the characteristic length scale. The trailing edge of the airfoil is placed at the origin in the two-dimensional coordinates. The airfoil is tilted by the angle of attack, α to the streamwise, x direction. The uniform flow U_∞ is enforced in the x direction at the outer boundaries. The Reynolds number based on L and U_∞ is chosen to be $10,000$. The inflow Mach number is altered from 0.1 to 0.6 to examine its effect on the flow stability.

For spatial discretization, a C-grid topology is employed by applying an optimized tri-diagonal sixth-order compact scheme to both convection and viscous terms, proposed by [5]. A standard fourth-order Runge-Kutta scheme is implemented for time advancement. The numerical domain is extended to $20L$ and $30L$ in the radial and downstream directions, respectively, with a non-reflecting boundary condition applied to all outer boundaries. The details of the implementation of numerical schemes and the verification studies of the present computational code are summarized in [4]. The number of grid cells is 1400 in the circumferential direction (600 around the airfoil surface; 800 in the wake region) and 200 in the wall normal direction, which leads to 2.8×10^5 cells in total. Grid convergence was confirmed by monitoring the resultant unsteady aerodynamic forces and the variance of velocity field on various grid sizes: the largest numerical grid employed in this grid dependence study contains more than 1×10^6 cells.

To quantitatively discuss the flow-instability mechanism, a linear stability analysis based on the Orr-Sommerfeld (O-S) equation is performed for the time-averaged velocity profiles obtained via the N-S solver described above, as will be shown in Section 4. From the time-averaged field, velocity components are extracted locally along the wall-normal direction from the airfoil surface on the suction side. At each location, an incompressible, parallel flow approximation is applied through local coordinate transformation. In discretizing the O-S equation in the wall normal direction, the Chebyshev colloca-

tion method is employed. For a given real frequency, the eigenvalue that provides the largest spatial growth is chosen at each streamwise location. Then, N factor is obtained by integrating the obtained spatial growth rate, or the imaginary part of a complex wave number along the airfoil surface, as was also done in [3].

3 Unsteady Field of Numerical Results

Since the main purpose of the present study is to examine the excitation condition of an acoustic feedback loop, the angle of attack should be small enough so that bulk separation does not occur near a leading edge (LE) to ensure the validity of two-dimensional assumption. Otherwise, laminar-turbulent transition should occur behind the separation to increase spanwise complexity; the acoustic feedback loop becomes less critical in a noise generation process. Unsteady motions arise for $\alpha \gtrsim 4.0°$ at this Reynolds number using the current simulation code. Here, we present the results of $\alpha = 4.5°$ and $\alpha = 5.0°$. By changing the inflow Mach number, the flow unsteadiness is apparently affected by both the acoustic disturbances, and the base-flow stability with a compressibility effect. As a computational parameter, the Mach number is altered by 0.1 for $\alpha = 4.5°$, and by 0.05 for $\alpha = 5.0°$, respectively, from 0.1 to 0.6. In the following, each case is labeled using its Mach number and angle of attack: for instance, the case at $M = 0.2$ and $\alpha = 4.5°$ is referred to as Case M20A45.

The instantaneous fields around the airfoil are presented in Figs. 2 and 3 for the given two angles of attack. At lower Mach numbers, $M \leq 0.2$, the wake instability is dominant to prompt the unsteadiness at $\alpha = 4.5°$, as each pair of vortices is shed into the wake with opposite signs of vorticity, ω. However, by slightly increasing α, due to an intensified adverse pressure gradient, the instability in the boundary layer becomes highly visible to form vortical motions on the suction side, as shown in Fig. 3, Case M20A050. This can be considered to be the onset of an acoustic feedback loop by altering the angle of attack. The stability analysis using the obtained velocity
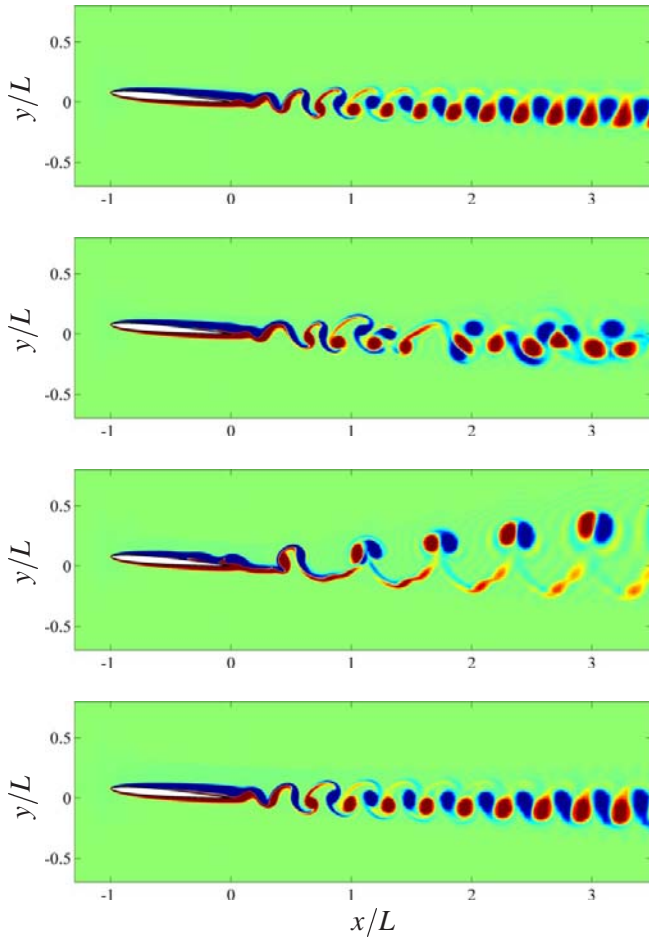
Fig. 2 Instantaneous vorticity field for $M = 0.2$, 0.3, 0.4, and 0.5 from top to bottom, respectively, at $\alpha = 4.5°$. Color scaling ranges from blue to red for $-4.0 \leq \omega L/U_\infty \leq +4.0$.
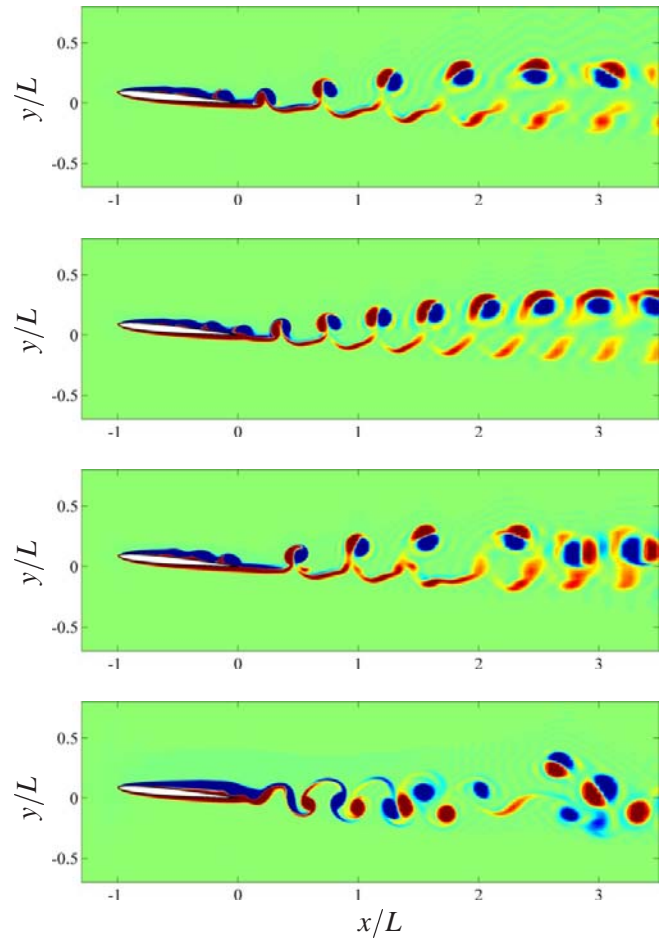
Fig. 3 Instantaneous vorticity field for $M = 0.2$, 0.25, 0.3, and 0.6 from top to bottom, respectively, at $\alpha = 5.0°$. See the caption of Fig. 2 for color scaling.

profiles will be presented in Section 4.

The present observation on the onset of the feedback loop is somewhat different from that reported in [3], where the acoustic feedback loop was prompted at a higher Mach number. However, as shown in Fig. 2, also by increasing M to 0.4, a flow state very similar to Case M20A50 is achieved in Case M40A45. The scattered pressure fluctuation p' has a Mach number dependence of $M^{1/2}$; in addition, the acoustic component of velocity fluctuations is comparable with $p'M$. Therefore, the increase in M amplifies the acoustic disturbances emitted from TE, affecting hydrodynamic instability. This excites a more unstable mode in the boundary layer, which eventually intensifies the scattered acoustic disturbances, too. Therefore, the organization of an acoustic feedback loop is regarded to be the self-induced resonance between the boundary layer instability mechanism and the acoustic disturbances scattered from TE.

However, by further increasing M to 0.5 as shown in Fig. 2, Case M50A45, the vortical motion is suppressed in the boundary layer, and again the flow unsteadiness seems dominated by the wake instability to reach periodicity with a frequency higher than that of Case M40A45. This is presumably due to the stabilization of the shear layer by adding compressibility effects. Likewise, in Case M60A45, a Karman vortex shedding is obtained in the wake with a slightly lower frequency than M50A45, although not presented in the figures. Similar stabilization is seen in Fig. 3 at $M = 0.6$, Case M60A50. Vortical motion is primarily formed behind TE, not in the boundary layer, although the flow is not periodic in this case.

In Fig. 2, before reaching the acoustic feedback loop sufficiently recognized at $M = 0.4$, a somewhat intermediate state is obtained in Case M30M45. The wake vortex pattern seems irregular and aperiodic. However, by performing a spectral decomposition on the temporal variation of a velocity field, many sharp line spectra are observed. Therefore, the obtained field can be regarded as the superposition of multiple discrete modes. The spectrum analysis of this case is pre-

Table 1 Normalized primary frequencies f^* for time-periodic cases at $\alpha = 4.5°$.

M	0.1	0.2	0.3	0.4	0.5	0.6
f^*	3.27	3.27	1.71†	1.53	2.86	2.55

†: Primary frequency chosen among multiple discrete line spectra.

Table 2 Normalized primary frequencies f^* for time-periodic cases at $\alpha = 5.0°$.

M	0.1	0.15	0.2	0.25
f^*	1.93	1.88	1.81	2.28

sented later in this section.

At $\alpha = 5.0°$, the acoustic feedback loop is achieved likewise at $M \leq 0.2$. However, at $M = 0.25$, Case M25A50, the shedding frequency discontinuously changes. This implies that the time-harmonic motions exist only with discrete modes, if incorporated with the acoustic feedback loop. Presumably, by increasing M from 0.2 to 0.25, the acoustic resonance moves to an adjoining mode with a higher frequency. The presence of discrete modes is due to the phase conformation requirement, as discussed in [7], between a hydrodynamic unstable wave and an acoustic wave at both edges of airfoil, if the acoustic disturbance is received in the boundary layer at LE. However, by increasing M furthermore, the flow shifts into an aperiodic state without settling in one discrete mode. At this angle of attack, the periodicity is never retrieved for $0.3 \leq M \leq 0.6$. The issue on the phase requirement is discussed again in Section 5.

The frequencies of each case that reaches a periodic vortex shedding is summarized in Tables 1 and 2, normalized with U_∞/L, expressed as f^*. In most cases, only the primary frequency appears in spectral decomposition, except its higher harmonics. However, in Case M30A45, multiple discrete line spectra are observed. The primary frequency given in Table 1 is determined from the velocity fluctuations sampled at $(x,y) = (0,L)$ in this case. In fact, the spectral decomposition of the far-field sound pressure also shows
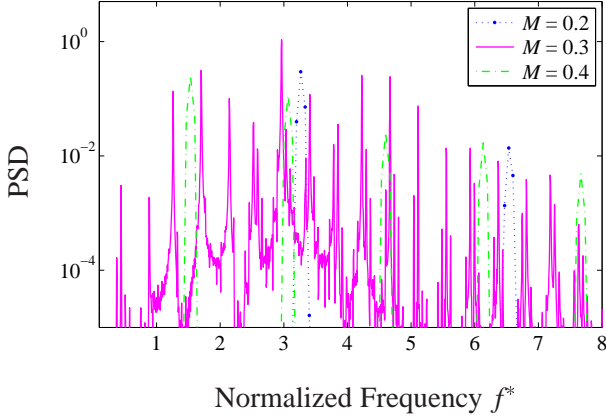
Fig. 4 Power spectral density of *v*-velocity sampled at $0.1L$ downstream from TE for $\alpha = 4.5°$.

Fig. 5 Power spectral density of *v*-velocity sampled at $0.1L$ downstream from TE for $\alpha = 5.0°$.

its peak at this frequency. In Fig. 4, the power spectral density is shown sampled in the wake region near TE, for Cases M20A45, M30A45, and M40A45. In the discrete spectral distributions of Case M30A45, the primary frequency is observed at $f^* \simeq 3.0$, different from that denoted in Table 1, while $f^* = 1.71$ stays secondary. This is supposedly due to the wake instability in the TE neighborhood; the self-induced frequency determined by the wake profile becomes prominent only locally just behind TE. However, the frequency $f^* = 1.71$ approximately corresponds to the most amplified frequency determined by the stability analysis of the boundary layer, which is dominant in the acoustic field. Similar observation is also reported in [3].

At $\alpha = 5.0°$, a periodic state is only obtained for lower Mach numbers. For $M \geq 0.3$, the spectrum of temporal field variations is shifted to a broadband distribution. However, the presence of several narrowband peaks can be recognized. In Fig. 5, the power spectral density is also shown for Cases M30A50 and M60A50, superposed on lower Mach number cases. The diagram of Case M30A50 clearly shows the primary and secondary peaks near the peaks at $M = 0.2$ and 0.25; the third peak is also found with a slightly higher frequency. These profiles imply that the aperiodic motions of M30A50 are weakly coupled with the multiple discrete modes of the acoustic feedback loop, extracted from broadband fluctua-
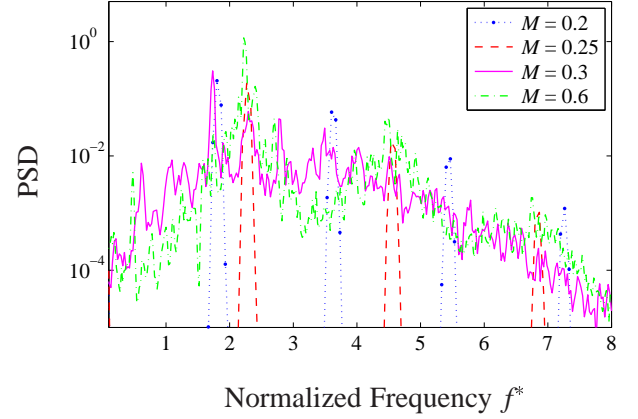
tions. On the other hand, Case M60A50 shows a distinguished primary mode observed at $f^* \simeq 2.2$ with several subsidiary modes. This primary frequency is considered to be an indication of the wake-flow instability, through the suppression of the boundary-layer fluctuations as shown in Fig. 3.

4 Onset Conditions of Acoustic Feedback Loop

The onset of an acoustic feedback loop was illustrated graphically in the instantaneous velocity field, as shown in Figs. 2 and 3. The excitation of the boundary-layer instability is considered to be the resonance between the acoustic wave scattering from TE, and the amplification of unstable waves in the suction-side boundary layer, which is essentially equivalent to, but presents a more simple mechanism than, that reported in high-Reynolds number experiments [e.g., 8]. The transition from the wake-induced vortex shedding, to the unsteadiness driven by the acoustic resonance, can also be seen in the pressure field. Fig. 6 presents the sound pressure scattered from the airfoil, and compares its magnitudes, with or without an acoustic feedback loop. By including the Mach number dependence, the sound pressure is intensified almost by an order of magnitude by prompting the boundary layer instability to achieve an acoustic feedback loop, either by increasing M or
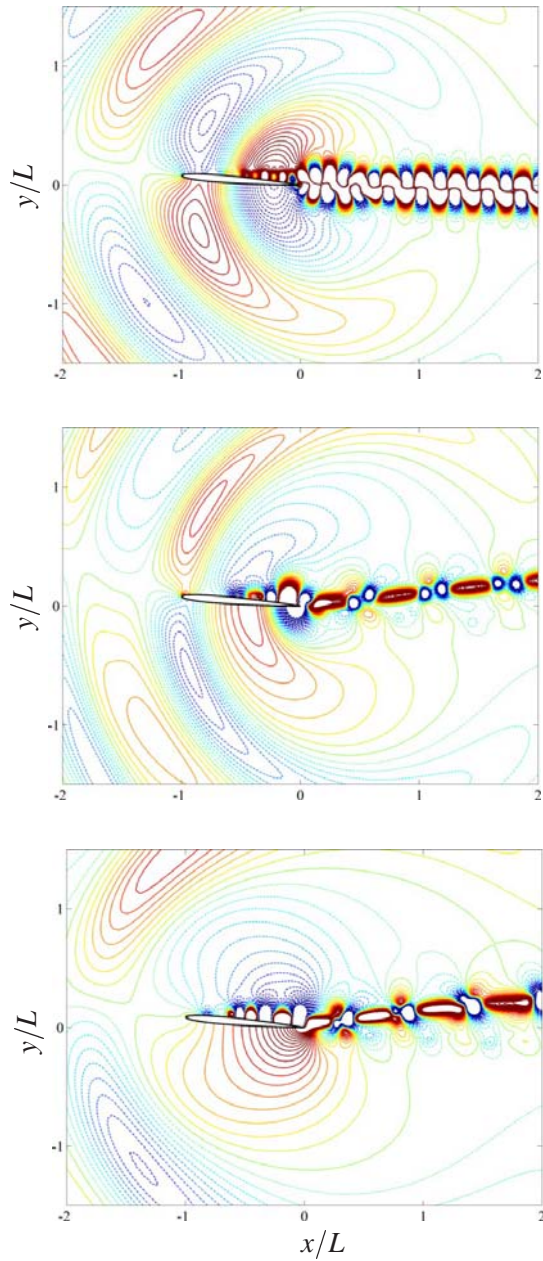
Fig. 6 Instantaneous pressure fluctuations $p'/(\rho_\infty U_\infty^2)$ around the NACA0006 airfoil for $M = 0.2$ (*top*) and $M = 0.4$ (*middle*) at $\alpha = 4.5°$, and $M = 0.2$ at $\alpha = 5.0°$ (*bottom*). The pressure field is weighted by the factor $(0.2/M)^{1/2}$ to remove the Mach number effect in sound pressure scattering at $M = 0.4$. One contour level denotes 2.0×10^{-5}, 2.0×10^{-4} and 2.0×10^{-4} from top to bottom, respectively.
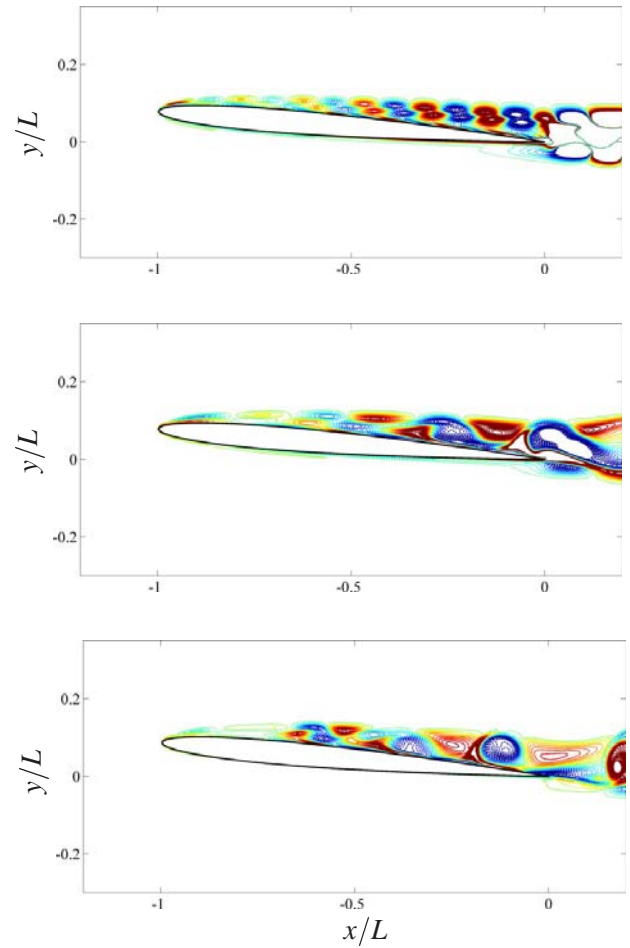
Fig. 7 Instantaneous vorticity fluctuations $\omega'L/U_\infty$ developing in the boundary layer of the NACA0006 airfoil for $M = 0.2$ (*top*) and $M = 0.4$ (*middle*) at $\alpha = 4.5°$, and $M = 0.2$ at $\alpha = 5.0°$ (*bottom*). One contour level denotes 2.5×10^{-2}, 6.0×10^{-1}, and 1.5 from top to bottom, respectively.
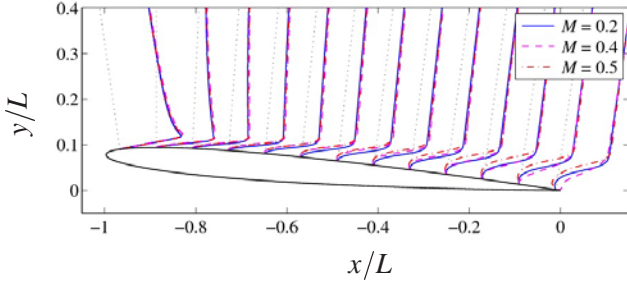
Fig. 8 Time-averaged tangential velocity profiles sampled in the wall normal directions in the boundary layer on suction side at $\alpha = 4.5°$ at various Mach numbers.
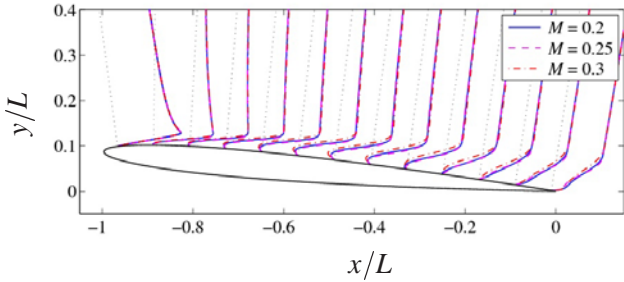

Fig. 9 Time-averaged tangential velocity profiles at $\alpha = 5.0°$. See the caption in Fig. 8.

Fig. 10 N factor distributions at 50% and 70% chord lengths for: $\circ$, $\alpha = 5.0°$; $*$, $\alpha = 4.5°$, computed using the time-averaged velocity profiles at $M = 0.2$ in each case.

α. Fig. 6 also captures the pressure fluctuation caused by the unstable waves developing in the suction side boundary layer in all three cases; however, the cases with the feedback-loop excitation show much intensified variations. Similar observations apply in the vorticity fluctuations, presented in Fig. 7. The development of vortical motions in the boundary layer represents the amplification of hydrodynamic unstable waves. Clearly, these vortices originate from the leading edge, convecting downstream with boundary-layer growth. There are no discernible waves in the pressure-side boundary layers, as mentioned above. The vortices in Case M20A50 grow very rapidly from the middle of the chord, which indicates a strong unstable mechanism in this region.

The adverse pressure gradient causes a separation bubble, as well as inflection points in the velocity profile in the upper-side boundary layer. This results in the shear-layer instability that amplifies the hydrodynamic waves at certain frequencies. Figs. 8 and 9 show the time-averaged velocity profiles at $\alpha = 4.5°$ and $\alpha = 5.0°$, re-

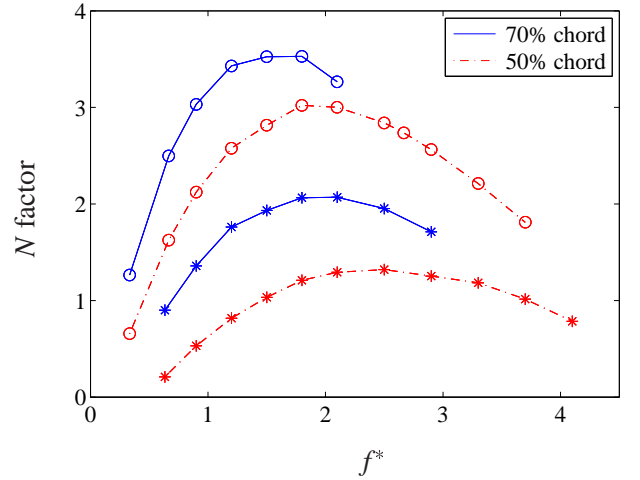spectively. Case M20A45 in Fig. 8 has a separation at about 50% chord length; then, the recirculation zone moderately extends down to the wake, where the vortex shedding starts to develop. Higher Mach number cases present separation bubbles larger than that of Case M20A45, although a fuller profile is obtained near TE in Case M40A45, due to the vortex mixing induced by the boundary-layer instability. It is also of interest that Case M50A45 poses more unstable profiles than lower M cases, despite the fact that its vortex shedding is supposedly dominated by the wake instability, as shown in Fig. 2. On the other hand, as shown in Fig. 9, the angle of attack increased only slightly leads to an earlier separation at about 10% chord, which imposes more intensified reverse flow region in the middle of the chord. This causes a faster growth of unstable waves in the boundary layer, as was also shown in Fig. 7. In addition, it should be noted that the difference between Cases M20A50 and M25A50 is almost unrecognizable in their time-averaged velocity profiles. Therefore, the frequency characteristics of flow stability should be identical in these two cases, although the resultant shedding frequencies are different as shown in Table 2.

Here, the results of a linear stability analysis using the O-S equation are presented. In obtain-

ing N factors, the integration is started at 10% chord. Since the vortical motion has well developed in the TE neighborhood where non-linearity would be significant in the cases at $\alpha = 5.0°$, the integration is interrupted at 70% chord; in addition, a negative spatial amplification also aborts the integration when obtained in an eigenvalue search. In Fig. 10, the N factors are compared for Cases M20A45 and M20A50, integrated to 50% and 70% chord lengths. Case M20A50 shows a greater amplification of unstable waves, as also predicted by the velocity profiles with an enhanced reverse flow in Fig. 9.

The most amplified frequency of Case M20A50 corresponds to $f^* \simeq 1.8$ at both 50% and 70% chord, which well approximates the resultant frequency. However, the frequency $f^* \simeq 2.3$ observed in Case M25A50 apparently provides less amplification, which does not follow a conventional rationale on frequency determination. The reason of the inconsistency could be explained as follows: as Case M30A50 shows aperiodic motions with a broadband character, if the magnitude of acoustic disturbances exceeds some threshold by increasing M, the vortical motions amplified in the boundary layer would not be able to maintain a stable periodic state beyond some limit, when shed into wake. However, in the lower Mach number case M25A50, the periodic state could be sustained, still by selecting a less unstable mode, which incidentally leads the vortical motions in the boundary layer to an optimized level at TE. In fact, this mode is shown to be a secondary choice in Case M30A50, as presented in Fig. 5. On the other hand, the most amplified frequency of Case M20A45 is approximately $f^* \simeq 2.0$ at 70%. It is slightly higher than the frequency actually obtained in Cases M30A45 and M40A45 with the acoustic feedback loop excited, nevertheless, still in a close range. The frequency $f^* \simeq 3.3$ in Case M20A45, determined by the wake instability, is also at a super-critical state, and shows a very moderate growth of unstable waves in the boundary layer as portrayed in Fig. 7, which does not significantly affect the vortex development in the wake.
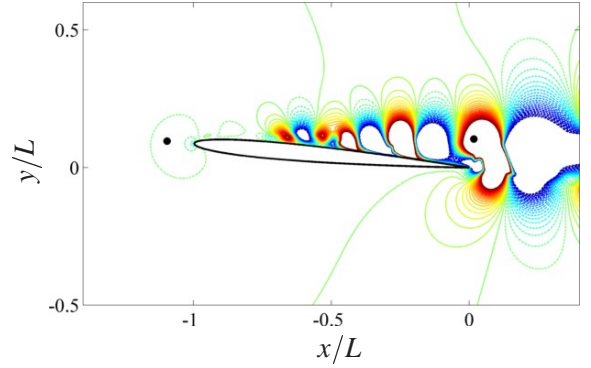

Fig. 11 Sampling locations of cross-covariance indicated by bullets (●) near both edges of the foil, superposed on instantaneous v-velocity fluctuation contours at $M = 0.1$. One contour level denotes $2.5 \times 10^{-2} U_\infty$.

5 Phase Requirement on Feedback Process

For the feedback process via acoustic wave scattering to perform effectively, correct phasing must be attained with the convection of hydrodynamic disturbances. This requirement of phase consistency yields the discrete spectral tones, either as multiple tonal peaks held simultaneously in Cases M30M45 and M30M50, or unique tones observed in the cases for $0.1 \leq M \leq 0.25$ at $\alpha = 5.0°$, as shown in Figs. 4 and 5. In this section, the phasing condition is examined for the cases at $\alpha = 5.0°$, where the feedback loop shows a common unique mode for $0.1 \leq M \leq 0.2$, and a higher-frequency mode at $M = 0.25$.
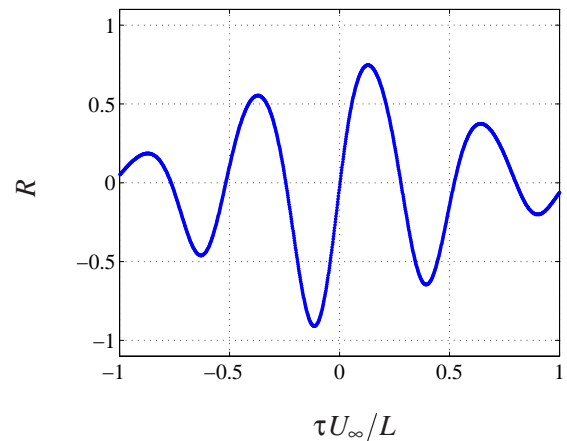

Fig. 12 Cross-covariance coefficient at $M = 0.1$.

As presented in Fig. 7, unstable waves are generated at LE, where an acoustic wave is converted into the hydrodynamic fluctuation, while the acoustic disturbance is emitted from TE, due to its geometrical singularity. First, to quantitatively describe the phase difference between TE and LE, we employ the cross covariance analysis of temporal velocity variation. By defining $v_i(t)$ and $v_j(t)$ as the velocity sampled in the neighborhood of TE and LE, and σ_i and σ_j as their variance, respectively, the cross covariance coefficient can be defined as

$$R(\tau) = \frac{\overline{\left(v_i(t+\tau) - \overline{v_i(t)}\right)\left(v_j(t) - \overline{v_j(t)}\right)}}{\sigma_i \sigma_j}, \quad (1)$$

where the overbar in the equation indicates taking time average. As in Eq. (1), R is the function of τ, the time difference between two points, if a time-varying field is sufficiently developed from its initial state. In Fig. 11, the sampling locations are denoted on the distributions of instantaneous v-velocity fluctuations: they are located at $0.1L$ apart vertically from TE, and $0.1L$ upstream from LE, respectively. Hydrodynamic vortical contributions are dominant in the velocity fluctuation at the TE-neighboring point, while the acoustic component is presumably a primary factor at the location apart from the LE-surface. Since the primary acoustic component in the velocity fluctuations is v velocity in the LE neighborhood due to the diffraction effect, v is chosen for the cross-covariance analysis applied in Eq. (1). The distribution of the cross-covariance coefficient of Case M10A50 is presented in Fig. 12. As can be seen in the figure, R shows its minimum at $\tau \simeq -0.1L/U_\infty$, which represents the phase-time difference between the two sampling locations. In fact, since the time variations are not random in the present time-periodic case, the resultant cross covariance depends on the sampling time length. However, it is confirmed that the phase-time difference defined above is not affected significantly by the time length.

For $0.1 \leq M \leq 0.2$, other than the three cases presented in Table 1, $M = 0.18$ is added in the following phase analysis. In Fig. 13, the normal-
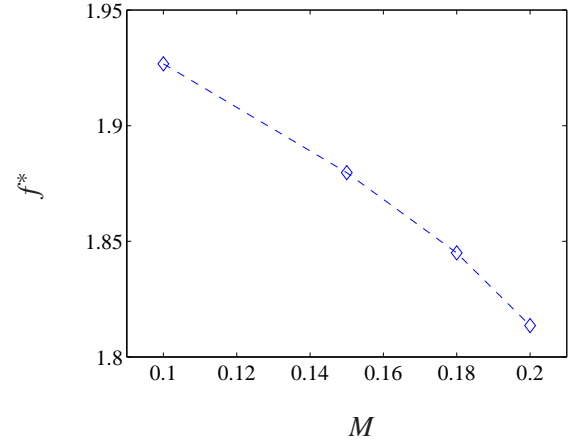

Fig. 13 Primary frequencies at $\alpha = 5.0°$ in the same resonance mode.

ized primary frequency f^* is shown at each Mach number. The number of unstable waves N_c on the chord length L can be estimated as

$$N_c = \frac{L f(M)}{U_c}, \quad (2)$$

where U_c is the phase velocity of unstable waves, and assumed to be constant here. Since the difference of N_c causes a phase shift between different Mach numbers, the phase-time difference $\Delta\tau$ from $M = 0.1$ can be written as follows for each Mach number:

$$\Delta\tau = \frac{N_c - N_c|_{M=0.1}}{f(M)} = \frac{L}{U_c}\left[1 - \frac{f(0.1)}{f(M)}\right]. \quad (3)$$

In addition, since the cases considered here supposedly belong to the same resonance mode, the increase of M causes the delay of LE phase due to acoustic-wave propagation. The time delay, considering an advection effect of mean flow, is represented as the retarded time t_{ret}:

$$t_{\text{ret}} = -\frac{L}{c_\infty(M) - U_\infty}, \quad (4)$$

where c_∞ is the sound velocity in a uniform field. Then, the phase difference $\Delta\phi$ from $M = 0.1$, caused by the variation of t_{ret}, can be expressed as

$$\Delta\phi = 2\pi\left[f(M)t_{\text{ret}} - f(0.1)t_{\text{ret}}|_{M=0.1}\right]. \quad (5)$$

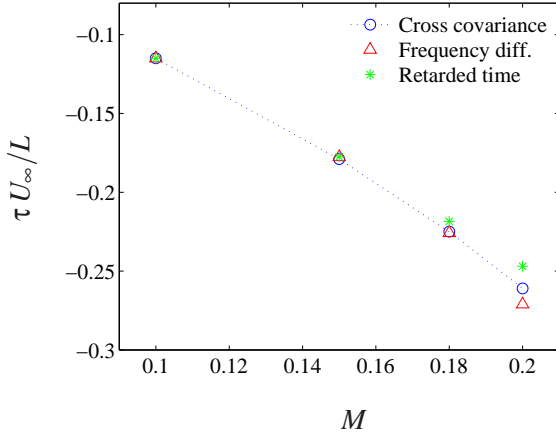**Fig. 14** Phase-time difference at various Mach numbers. ○, estimated from cross covariance; △, frequency difference, Eq. (3); ∗, retarded time of a sound wave Eq. (6).

Fig. 15 The comparison of discrete modes predicted by Eq. (8) ($3 \leq m \leq 7$) and the frequencies obtained in the present study.

From Eq. (5), the phase-time difference associated with the retarded time can be derived as

$$\Delta \tau = t_{\text{ret}} - \frac{f(0.1)}{f(M)} t_{\text{ret}}\big|_{M=0.1}. \qquad (6)$$

Now by using Eqs. (3) and (6), we can compare the phase difference between TE and LE, from two different, acoustic and hydrodynamic waves, with different phase velocities. Here we assume the phase velocity of an unstable wave in a boundary layer as $U_c = 0.4U_\infty$, which corresponds to that reported in [8], and reasonably approximates the result of the linear stability analysis. In Fig. 14, the phase-time differences are presented, estimated from the cross-covariance minima, and also from the above equations. As can be seen, these three different estimations agree well, except a small deviation at $M = 0.2$. This indicates that, by increasing M, the resultant phase delay due to the sound propagation is reflected in lowering the vortex-shedding frequency to maintain the feedback loop. It is also supported by the measured phase differences that coincide with the estimations employing Eqs. (3) and (6), by using the cross-covariance analysis. Therefore, once an acoustic resonance of boundary-layer instability is achieved, it requires a phase consistency between acoustic and unstable waves to maintain the feedback loop, even if
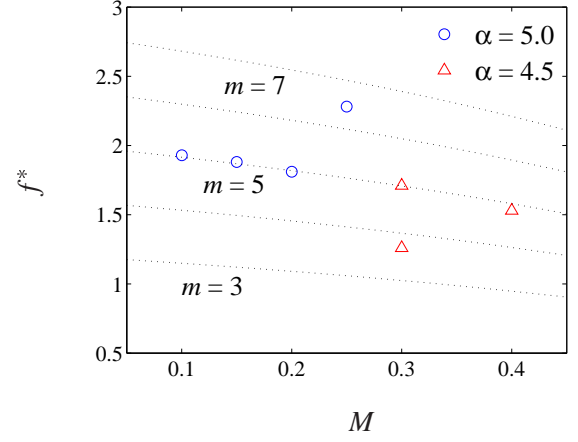
the Mach number is altered.

Through the discussion above, by equating Eqs. (3) and (6), we can derive a relation on a frequency dependence:

$$\left[\frac{1}{U_c} + \frac{1}{c_\infty(M) - U_\infty} \right] L f(M) = const. \qquad (7)$$

This equation indicates that the total number of waves existing on an airfoil does not vary on the Mach number in a resonance mode. However, in the study of [7], a similar relation was presented as an assumption:

$$\left[\frac{1}{U_c} + \frac{1}{c_\infty(M) - U_\infty} \right] L f(M) = m, \qquad (8)$$

where m is an integer that indicates the discrete mode: this requires that the sum of the number of both acoustic and hydrodynamic waves, must be an integer to attain an acoustic feedback loop. On the frequencies obtained in the present study, the validity of Eq. (8) is examined in Fig. 15. In addition to the primary modes given in Tables 1 and 2, the secondary mode of Case M30A45 is also presented. The cases studied above on the phasing condition, and also the primary frequencies at $\alpha = 4.5°$ for $M = 0.3$ and 0.4, agree very well with the mode at $m = 5$. However, Case M25A50 and the secondary frequency of Case M30A45 show the non-negligible deviation from the integer modes predicted by Eq. (8). The reason of

this inconsistency is not clear here. However, in Eq. (8), it is assumed that the phase should be continuous across two different waves at TE, where the vortices are well developed, and therefore, non-linear effects cannot be ignored, which may not ensure the phase continuity at TE. Also, the sound source of TE noise is usually regarded to be the vortices located in the neighborhood of TE; the acoustic phase should be determined by considering the total effects from all those vortices, not solely from the phase of an unstable wave arriving at TE.

6   Conclusion

In the present study, the onset condition of an acoustic feedback loop was investigated numerically by using both the higher-order compressible flow solver and the linear stability analysis. A parametric study of the flow Mach number was conducted by employing two angles of attack, $\alpha = 4.5°$ and $5.0°$, which provide different sizes of separation bubbles on the suction side, and therefore, different stability characteristics. By increasing M, the amplified acoustic disturbance prompted the feedback loop first at $\alpha = 4.5°$; but also the shear layer seemed to be stabilized at even higher Mach numbers, which prevents the feedback loop, retrieving a wake-flow Karman vortex shedding, as seen in Case M50A45. For lower Mach number cases at $\alpha = 5.0°$, a phasing condition was examined to attain an acoustic feedback loop. By using the cases on the same resonance mode, phase differences were estimated using the cross covariance analysis. It was shown that the obtained phase difference agrees well with those determined by the retarded time of a sound wave, and also by the frequency difference.

It was confirmed that the multiple modes exist with the acoustic feedback loop at a low Reynolds number. Case M30A50 shows aperiodic motions with multiple narrowband peaks in a frequency domain. The primary frequency corresponds to that of lower Mach number cases. The secondary mode is also found in Case M25A50, which shows a unique mode that does

not coincide with the most amplified frequency. Using the frequencies obtained in the present study, the phasing condition proposed in [7] is examined. On a provided mode, the present data agree well with the estimated Mach number dependence. However, the frequency jump between two adjoining modes is not quantitatively well predicted. It is still an open question how these discrete modes are provided with a certain frequency width, which would be able to formulate the frequency determination mechanism of an acoustic feedback loop.

References

[1] R. Betchov and W. O. Criminale. Spatial instability of the inviscid jet and wake. *Phys. Fluids*, 9(2):359–362, 1966.

[2] G. Desquesnes, M. Terracol, and P. Sagaut. Numerical investigation of the tone noise mechanism over laminar airfoils. *J. Fluid Mech.*, 591:155–182, 2007.

[3] T. Ikeda, T. Atobe, and S. Takagi. A numerical study of the trailing-edge noise generated from a thin airfoil and its flow stability. In *The 58th National Congress of Theoretical and Applied Mechanics*, 1F03, Tokyo, Japan, 2009.

[4] T. Ikeda, T. Sumi, and T. Kurotaki. Interface conditions of finite difference compact schemes for computational aeroacoustics. *AIAA J.*, 47(11):2658–2665, 2009.

[5] J. W. Kim and D. J. Lee. Optimized compact finite difference schemes with maximum resolution. *AIAA J.*, 34(5):887–893, 1996.

[6] W. Koch. Local instability characteristics and frequency determination of self-excited wake flows. *J. Sound Vib.*, 99(1):53–83, 1985.

[7] R. E. Longhouse. Vortex shedding noise of low tip speed, axial flow fans. *J. Sound Vib.*, 53(1):25–46, 1977.

[8] E. C. Nash, M. V. Lowson, and A. McAlpine. Boundary-layer instability noise on aerofoils. *J. Fluid Mech.*, 382:27–61, 1999.

[9] R. W. Paterson, P. G. Vogt, M. R. Fink, and C. L. Munch. Vortex noise of isolated airfoils. *J. Aircraft*, 10(5):296–302, 1973.

[10] A. Roshko. On the wake and drag of bluff bodies. *J. Aero. Sci.*, 22(2):124–130, 1955.

[11] R. D. Sandberg, L. E. Jones, N. D. Sandham, and P. F. Joseph. Direct numerical simulations of tonal noise generated by laminar flow past airfoils. *J. Sound Vib.*, 320:838–858, 2009.

[12] C. K. W. Tam. Discrete tones of isolated airfoils. *J. Acoust. Soc. Am.*, 55(6):1173–1177, 1974.

Copyright Statement